

# STRINGENT LIMITS ON THE POLARIZED SUBMILLIMETER EMISSION FROM PROTOPLANETARY DISKS

A. MEREDITH HUGHES<sup>1</sup>, DAVID J. WILNER<sup>1</sup>, JUNGYEON CHO<sup>2,3</sup>, DANIEL P. MARRONE<sup>4,6</sup>, ALEXANDRE LAZARIAN<sup>3</sup>,  
 SEAN M. ANDREWS<sup>1,7</sup>, AND RAMPRASAD RAO<sup>7</sup>

<sup>1</sup> Harvard-Smithsonian Center for Astrophysics, 60 Garden Street, Cambridge, MA 02138, USA; [mhughes@cfa.harvard.edu](mailto:mhughes@cfa.harvard.edu), [dwilner@cfa.harvard.edu](mailto:dwilner@cfa.harvard.edu),  
[sandrews@cfa.harvard.edu](mailto:sandrews@cfa.harvard.edu)

<sup>2</sup> Department of Astronomy and Space Science, Chungnam National University, Daejeon, Republic of Korea; [jcho@cnu.ac.kr](mailto:jcho@cnu.ac.kr)

<sup>3</sup> University of Wisconsin, Department of Astronomy, 475 N. Charter Street, Madison, WI 53706, USA; [lazarian@astro.wisc.edu](mailto:lazarian@astro.wisc.edu)

<sup>4</sup> The University of Chicago, The Kavli Institute for Cosmological Physics, 933 East 56th Street, Chicago, IL 60637, USA; [dmarrone@oddjob.uchicago.edu](mailto:dmarrone@oddjob.uchicago.edu)

<sup>5</sup> Institute of Astronomy and Astrophysics, Academia Sinica, 7F of Condensed Matter Sciences and Physics Department Building, National Taiwan University,  
 No. 1 Roosevelt Rd, Sec. 4 Taipei 10617, Taiwan; [r Rao@asiaa.sinica.edu.tw](mailto:r Rao@asiaa.sinica.edu.tw)

Received 2009 June 25; accepted 2009 September 8; published 2009 September 30

## ABSTRACT

We present arcsecond-resolution Submillimeter Array (SMA) polarimetric observations of the 880  $\mu\text{m}$  continuum emission from the protoplanetary disks around two nearby stars, HD 163296 and TW Hydrae. Although previous observations and theoretical work have suggested that a 2%–3% polarization fraction should be common for the millimeter continuum emission from such disks, we detect no polarized continuum emission above a  $3\sigma$  upper limit of 7 mJy in each arcsecond-scale beam, or  $<1\%$  in integrated continuum emission. We compare the SMA upper limits with the predictions from the exploratory Cho & Lazarian model of polarized emission from T Tauri disks threaded by toroidal magnetic fields, and rule out their fiducial model at the  $\sim 10\sigma$  level. We explore some potential causes for this discrepancy, focusing on model parameters that describe the shape, magnetic field alignment, and size distribution of grains in the disk. We also investigate related effects like the magnetic field strength and geometry, scattering off of large grains, and the efficiency of grain alignment, including recent advances in grain alignment theory, which are not considered in the fiducial model. We discuss the impact each parameter would have on the data and determine that the suppression of polarized emission plausibly arises from rounding of large grains, reduced efficiency of grain alignment with the magnetic field, and/or some degree of magnetic field tangling (perhaps due to turbulence). A poloidal magnetic field geometry could also reduce the polarization signal, particularly for a face-on viewing geometry like the TW Hya disk. The data provided here offer the most stringent limits to-date on the polarized millimeter-wavelength emission from disks around young stars.

**Key words:** circumstellar matter – planetary systems: protoplanetary disks – polarization – stars: individual (HD 163296, TW Hydrae)

*Online-only material:* color figures

## 1. INTRODUCTION

The magnetic properties of circumstellar disks are central to a wide range of physical processes relevant for planet formation. Dust and gas transport and mixing (e.g., Ciesla 2007), meteoritic composition (e.g., Boss 2004), disk chemistry (e.g., Semenov et al. 2006), and the migration of planetary embryos through the disk (e.g., Chambers 2006) are all thought to be influenced by magnetohydrodynamic (MHD) turbulence. But perhaps the greatest impact of a magnetized disk is that MHD turbulence can provide the source of viscosity that drives disk evolution. Since the seminal work by Lynden-Bell & Pringle (1974), the photospheric excess and variability exhibited by pre-main-sequence stars have been attributed to an accretion disk. The viscous transport mechanism that supports the accretion process can also explain many aspects of the time evolution of circumstellar disks (Hartmann et al. 1998), and by extension can help to constrain the physical conditions and timescales relevant for planet formation. However, there are remarkably few observational constraints on the magnitude and physical origin of viscosity in circumstellar disks.

As conjectured by Shakura & Sunyaev (1973), turbulence can provide large enough viscosities to account for accretion and

disk evolution on the appropriate timescales. The mechanism most commonly invoked as the source of this turbulence is the magnetorotational instability (MRI), in which magnetic interactions between fluid elements in the disk combine with an outwardly decreasing velocity field to produce torques that transfer angular momentum from the inner disk outward (Balbus & Hawley 1991, 1998; see also Velikhov 1959 and Chandrasekhar 1960). Indeed, it is unlikely that turbulence in an unmagnetized, azimuthally symmetric Keplerian disk can sufficiently redistribute angular momentum: magnetic fields must be invoked to enable Shakura–Sunyaev viscosity (e.g., Balbus et al. 1996). The ionization fraction is likely high enough for magnetic coupling of material over much of the outer disk (see, e.g., Sano et al. 2000; Turner et al. 2007), and the observed Keplerian rotation of protoplanetary disks provides the requisite velocity shear. However, the magnetic field properties (strength and geometry) far from the central star remain unconstrained.

Resolved observations of polarized submillimeter continuum emission are uniquely suited to constrain the magnetic field geometry—independent of the disk structure—via the orientation of polarization vectors produced by dust grains aligned with the magnetic field (Aitken et al. 2002). In the presence of an anisotropic radiation field, irregularly shaped grains with different cross sections to left and right circular polarizations of light can be spun up to high speeds by radiative torques (e.g., Dolginov 1972; Dolginov & Mitrofanov 1976; Draine &

<sup>6</sup> Jansky Fellow

<sup>7</sup> Hubble Fellow

Weingartner 1996).<sup>8</sup> These spinning grains precess around magnetic field lines, and ultimately align with their long axes perpendicular to the local magnetic field direction. Polarized emission or absorption by these aligned grains can thus trace the magnetic field structure in dusty interstellar media (see Lazarian 2007, and references therein).

The first models of polarized emission from disks incorporating the radiative torque alignment mechanism have recently been calculated by Cho & Lazarian (2007). Using a two-layer Chiang et al. (2001) disk structure model threaded by a toroidal magnetic field (with circular field lines in the plane of the disk, centered on the star), they calculated the polarization emitted as a function of wavelength and position in the disk, incorporating emission and selective absorption mechanisms, but not scattering. They predict a 2%–3% polarization fraction at 850  $\mu\text{m}$ , and note that grain alignment is particularly efficient in the low-density outer disk regions. At millimeter wavelengths, dust grain opacities are low and optically thin thermal continuum emission primarily originates in the midplane where most of the mass is located. Polarimetric observations of millimeter-wavelength dust continuum emission therefore trace magnetic field geometry near the midplane in the outer disk, in regions where the magnetic field is strong enough for grains to become aligned and the density is low enough that grain spin-up is not impeded by gas drag.

The first attempt to observe polarized millimeter-wavelength emission from protoplanetary disks was made by Tamura et al. (1995, 1999). They used the James Clerk Maxwell Telescope (JCMT) to observe several young systems in the Taurus–Auriga molecular cloud complex—HL Tau, GG Tau, DG Tau, and GM Aur—and reported tentative ( $\sim 3\sigma$ ) detections of polarized millimeter-wavelength continuum emission from three of the four systems. The exception was GG Tau, for which they report a  $2\sigma$  upper limit of 3%. While the disks are unresolved in the 14'' JCMT beam, the approximate alignment of the GM Aur and DG Tau polarization vectors with the known orientation of the disk minor axis is suggestive of a globally toroidal magnetic field structure. However, finer resolution is required to confirm the magnetic field structure in the disks, and differentiate it from any potential contamination from an envelope or cloud material. DG Tau was followed up at a wavelength of 350  $\mu\text{m}$  using the Caltech Submillimeter Observatory by Krejny et al. (2009), and no polarization was detected with an upper limit of  $\sim 1\%$ . They suggest that the decrease of polarization percentage relative to the tentative 850  $\mu\text{m}$  detection and the corresponding Cho & Lazarian (2007) prediction at 350  $\mu\text{m}$  may be due to some combination of polarization self-suppression—effectively an absorption optical depth effect (see e.g., Hildebrand et al. 2000)—or increased scattering at shorter wavelengths, which would produce a signal orthogonal to that expected for a toroidal magnetic field. In summary, while the Cho & Lazarian (2007) predictions are consistent with the magnitude of the tentative JCMT detections, as discussed by Krejny et al. (2009), the predicted polarization spectrum is inconsistent with the 350 and 850  $\mu\text{m}$  observations of DG Tau.

In the absence of spatially resolved observations, the origin of the polarized emission in these systems remains unclear.

While the position angle of the polarized emission observed in the three systems in the Taurus–Auriga complex suggests association with the circumstellar disk, at least two of these sources (DG Tau and HL Tau) are flat-spectrum sources host to jets and likely retain envelope material that could aid in generating a polarization signal (e.g., Kitamura et al. 1996; D'Alessio et al. 1997). Tamura et al. (1995) suggest that the emission from HL Tau may arise from an interface region between the disk and a small envelope, and that the upper limit for GG Tau may be due to the lack of an envelope combined with weak, compact emission from the circumbinary ring. Observations of the GM Aur system using the NICMOS instrument on the *Hubble Space Telescope* (HST) indicate that it too may host a tenuous remnant outflow and envelope (Schneider et al. 2003). Nevertheless, with both theoretical predictions and observational evidence pointing to a 2%–3% polarization fraction at 850  $\mu\text{m}$  in several T Tauri disks, resolved observations revealing the magnetic field geometry should be possible with current millimeter interferometers for bright disks. At  $\sim 1''$  resolution, such data would be well matched to the size scales at which the polarization fraction is expected to be the largest in the context of the Cho & Lazarian (2007) models.

In order to test the Cho & Lazarian (2007) model predictions and constrain magnetic field strengths and geometries, we observed two nearby systems, HD 163296 and TW Hya, with the Submillimeter Array (SMA) polarimeter.<sup>9</sup> These targets were selected primarily for their large millimeter-wave fluxes to maximize the expected polarization signal. Unlike the previously observed Taurus targets, they are isolated from molecular cloud material. HD 163296 has a total flux of 1.92 Jy at 850  $\mu\text{m}$  (Mannings 1994), while TW Hya has a flux of 1.45 Jy at 800  $\mu\text{m}$  (Weintraub et al. 1989), predicting a total polarized flux of  $\sim 40$  mJy in each system. Polarization of this magnitude should be observable with the SMA even if resolved across a few beams. HD 163296 is a Herbig Ae star with a mass of  $2.3 M_{\odot}$  located at a distance of 122 pc (van den Ancker et al. 1998). It is surrounded by a flared disk viewed at an intermediate inclination of  $\sim 45^{\circ}$ , observed to extend to at least 500 AU in molecular gas and scattered light (Isella et al. 2007; Grady et al. 2000), which has been extensively observed and modeled at millimeter wavelengths (Mannings & Sargent 1997; Natta et al. 2004; Isella et al. 2007). TW Hya is a K star located at a distance of only 51 pc (Mamajek 2005; Hoff et al. 1998). It hosts a massive circumstellar disk viewed nearly face-on at an inclination of  $7^{\circ}$  and extending to a radius of  $\sim 200$  AU in molecular gas and scattered light (Qi et al. 2004; Roberge et al. 2005). It is also a prototypical example of the class of disks with infrared deficits in their spectral energy distribution, known as “transition” disks. It has been shown to have a central deficit of dust emission extending out to 4 AU (Calvet et al. 2002; Hughes et al. 2007), with a low mass accretion rate (Muzerolle et al. 2000) that may indicate clearing by a giant planet in formation (Alexander & Armitage 2007).

We describe our observations of these systems in Section 2 and present the upper limits in Section 3. In Section 4.1, we describe the initial predictions generated by the Cho & Lazarian (2007) models and compare these predictions to the SMA observations. We then use these initial models as a starting point for an exploration of parameter space that seeks to describe how the different factors affect the predicted polarization properties

<sup>8</sup> More recent research in Lazarian & Hoang (2007) shows that in many cases rather than being spun up paramagnetic grains get slowed down by radiative torques, which means that the grains aligned by radiative torques do not necessarily rotate suprathermally. Nevertheless, the maximal rotational rate provides a useful parameterization of the effect of the radiative torques as discussed in detail in Hoang & Lazarian (2008).

<sup>9</sup> The SMA is a joint project between the Smithsonian Astrophysical Observatory and the Academia Sinica Institute of Astronomy and Astrophysics and is funded by the Smithsonian Institution and the Academia Sinica.

**Table 1**  
Observational Parameters<sup>a</sup>

Parameter	HD 163296			TW Hya		
	Compact 2008 May 29	Extended 2008 July 12	C+E	Compact 25 Jan 2009	Extended 15 Feb 2009	C+E
340 GHz Continuum						
Beam size (FWHM)	2''.2 × 1''.3	0''.9 × 0''.7	1''.0 × 0''.9	4''.7 × 2''.0	1''.1 × 0''.8	1''.2 × 0''.8
P.A.	50°	−8°	7°	−1°	6°	6°
RMS noise (mJy beam <sup>−1</sup> )						
Stokes <i>I</i> <sup>b</sup>	11	7.8	5.7	35	6.8	5.5
Stokes <i>Q</i> & <i>U</i>	3.8	2.7	2.4	6.3	2.4	2.3
Peak flux density (mJy beam <sup>−1</sup> )						
Stokes <i>I</i>	996	639	739	990	450	474
Stokes <i>Q</i> & <i>U</i> (3σ upper limit)	<11	<8.1	<7.2	<19	<7.2	<6.9
Integrated flux <sup>c</sup> (Stokes <i>I</i> ; Jy)	1.65	1.79	1.64	1.24	1.33	1.26
CO(3-2) Line						
Beam size (FWHM)	2''.2 × 1''.4	0''.9 × 0''.7	1''.1 × 1''.0	5''.0 × 1''.2	1''.1 × 0''.7	1''.2 × 0''.7
P.A.	50°	−8°	17°	−1°	9°	9°
RMS noise (mJy beam <sup>−1</sup> )	25	19	15	55	14	13
Peak flux density (mJy beam <sup>−1</sup> )						
Stokes <i>I</i>	6500	2650	3730	1520	1800	3090
Stokes <i>Q</i> & <i>U</i> <sup>d</sup> (3σ upper limit)	<75	<57	<45	<170	<42	<39
Integrated flux <sup>e</sup> (Stokes <i>I</i> ; Jy km s <sup>−1</sup> )	110	56	95	47	13	27

**Notes.**

<sup>a</sup> All quoted values assume natural weighting.

<sup>b</sup> The rms in Stokes *I* is limited by a dynamic range rather than sensitivity.

<sup>c</sup> The integrated continuum flux is calculated using the MIRIAD task `uvfit`, assuming an elliptical Gaussian brightness profile.

<sup>d</sup> The rms for the line is calculated using a channel width of 0.7 km s<sup>−1</sup>.

<sup>e</sup> The integrated line flux is calculated by integrating the zeroth moment map inside the 3σ brightness contours.

(Section 4.2). We expand on these results by discussing the potential effects of physical mechanisms not included in the models (Section 4.3). In Section 5, we evaluate which physical conditions are most likely to contribute to the suppression of polarization relative to the fiducial model and summarize our results.

## 2. OBSERVATIONS AND DATA REDUCTION

Observations were conducted using the SMA polarimeter, described in detail in Marrone & Rao (2008). The polarimeter uses a set of quarter-wave plates to convert the normally linear SMA feeds to circular polarization. By rotating the wave plate between two orientations separated by 90°, a single linear feed can be converted into either of the circular bases (left and right, or *L* and *R*). Since only one polarization (*L* or *R*) can be sampled on any antenna at any given time, full sampling of all four polarization states (*LL*, *RR*, *RL*, and *LR*) for all baselines (numbering  $N(N-1)/2$ , where  $N$  is the number of antennas) must be accomplished by rotating the wave plates through a series of orientation patterns conveniently described by the two-state Walsh functions (see Marrone 2006). A full set of polarization states can be obtained for all baselines in ~5 minutes using a series of short (10 s) integrations with the wave plates rotated through patterns described by Walsh functions for the appropriate number of antennas. These 5 minute intervals of data are combined into quasi-simultaneous Stokes parameters for each baseline ( $I = (RR + LL)/2$ ,  $Q = (RL + LR)/2$ ,  $U = i(LR - RL)/2$ ,  $V = (RR - LL)/2$ ), where *I* measures the total intensity, *V* measures the intensity of circular polarization, and  $\sqrt{Q^2 + U^2}$  gives the total linearly polarized intensity, which can also be used to calculate the local fractional (or percent) linear polarization  $\sqrt{Q^2 + U^2}/I$ . Note

that the aligned states (*RR* and *LL*) separate the total intensity from the circularly polarized intensity, while the crossed states (*LR* and *RL*) provide information about the linearly polarized intensity. Of course, this represents an idealization. Two relevant non-ideal effects are (1) if the *R* and *L* gains are not perfectly matched, then some of the bright Stokes *I* flux can leak into Stokes *V* when the difference is taken between *LL* and *RR*, and (2) instrumental “leakage” of left circularly polarized light through a nominally right circularly polarized wave plate (and vice versa) can transfer Stokes *I* to the linear states *Q* and *U*.

Polarimetric SMA observations of the HD 163296 disk at 880 μm wavelength were carried out in the compact configuration on 2008 May 29, and in the extended configuration on 2008 July 12. The weather was excellent, with the 225 GHz opacity below 0.05 both nights, reaching as low as 0.03 on the night of 12 July. The phases were also extremely stable on both nights. The projected baseline lengths spanned a range of 9 to 260 kλ, providing a synthesized beam size of 1''.1 × 0''.89 for the combined data set, using natural weighting (see Table 1 for details). The quasar 3c454.3 was observed for 2.5 hr through more than 90° of parallactic angle during its transit in order to calibrate the complex leakages of the quarter-wave plates. The quasar J1733−130 was used to calibrate the atmospheric and instrumental gain, and the quasar J1924−292 was observed at 45 minute intervals throughout the night to test the quality of the phase transfer from J1733−130 as well as the calibration of the quarter-wave plate leakage. Uranus was used as the flux calibrator, yielding a flux for J1733−130 of 1.62 Jy on the night of May 29 and 2.01 Jy on the night of July 12. Uranus, Callisto, 3c273, and 3c279 were included as passband calibrators.

Observations of the disk around TW Hya were conducted in the subcompact and extended configurations of the SMA during the nights of 2009 January 25 and February 15, respectively.

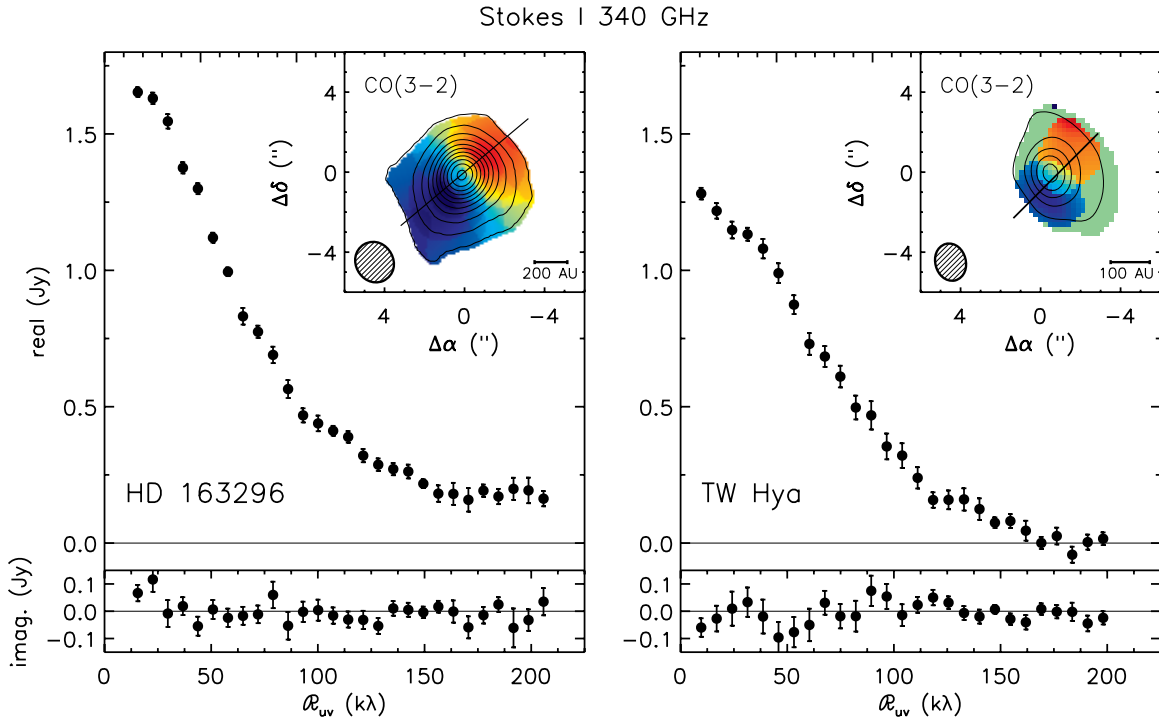


**Figure 1.** Real (top) and imaginary (bottom) Stokes  $I$  continuum visibilities for HD 163296 (left) and TW Hya (right) as a function of the distance from the disk center in the  $(u,v)$  plane, corrected for projection effects due to the inclination of the disk to our line of sight. Error bars show the standard error of the mean in each 7 k $\lambda$  bin. See Lay et al. (1997) for details of the deprojection process. The inset in the upper right of each plot shows the CO(3-2) moment maps in Stokes  $I$  for the two disks. The colors indicate the first moment (intensity-weighted velocity), and the contours show the zeroth moment (velocity-integrated intensity) in intervals of 3 Jy km s $^{-1}$ . The solid line marks the position angle of the disk as determined by Isella et al. (2007) and Qi et al. (2004). The size and orientation of the synthesized beam are indicated at the lower left of each moment map.

(A color version of this figure is available in the online journal.)

Due to the far southern declination of TW Hya in combination with the stringent elevation limits imposed to avoid antenna collisions in the subcompact configuration, the source was only observable for three hours on the night of January 25, while a full six hours of observations were obtained on February 15. The weather was again excellent, particularly for the extended configuration, during which the 225 GHz opacity remained stable between 0.03 and 0.04 for most of the night. The projected baseline lengths in the final data set varied from 6 to 250 k $\lambda$ , providing a synthesized beam size of  $1''.2 \times 0''.9$  in the final data set (see Table 1). The instrumental polarization was calibrated by observing 3c273 over 90° of parallactic angle for three hours across its transit. The quasar J1037–295 was used as the gain calibrator, and 3c279 was observed once per hour to test both the quality of the phase transfer and the instrumental polarization calibration. The primary flux calibrator was Titan, yielding a flux for J1037–295 of 0.64 Jy on the night of January 25 and 0.53 Jy on the night of February 15. 3c279, 3c273, and J1037–295 were included as passband calibrators.

The double sideband receivers were tuned to a central frequency of 340.75 GHz (880  $\mu$ m) for the HD 163296 observations and 341.44 GHz (877  $\mu$ m) for the TW Hya observations, with each 2 GHz wide sideband centered  $\pm 5$  GHz from that value. The correlator was configured to observe the CO(3-2) transition (rest frequency 345.796 GHz) with a velocity resolution of 0.70 km s $^{-1}$ . The data were edited and calibrated using the MIR software package,<sup>10</sup> while the standard tasks of Fourier transforming the visibilities, deconvolution with the CLEAN algorithm, and restoration were carried out using the

MIRIAD software package. For a summary of the observational parameters, including the  $3\sigma$  upper limits in Stokes  $Q$  and  $U$  for the individual tracks and the combined data sets, refer to Table 1. The test quasars for all tracks were point-like and unresolved. We detect polarized emission from the test quasars independently in each data set with a polarization fraction of between 8% and 12% and a direction consistent between lower and upper sidebands, as expected for linearly polarized emission from quasars at these wavelengths (see Marrone 2006).

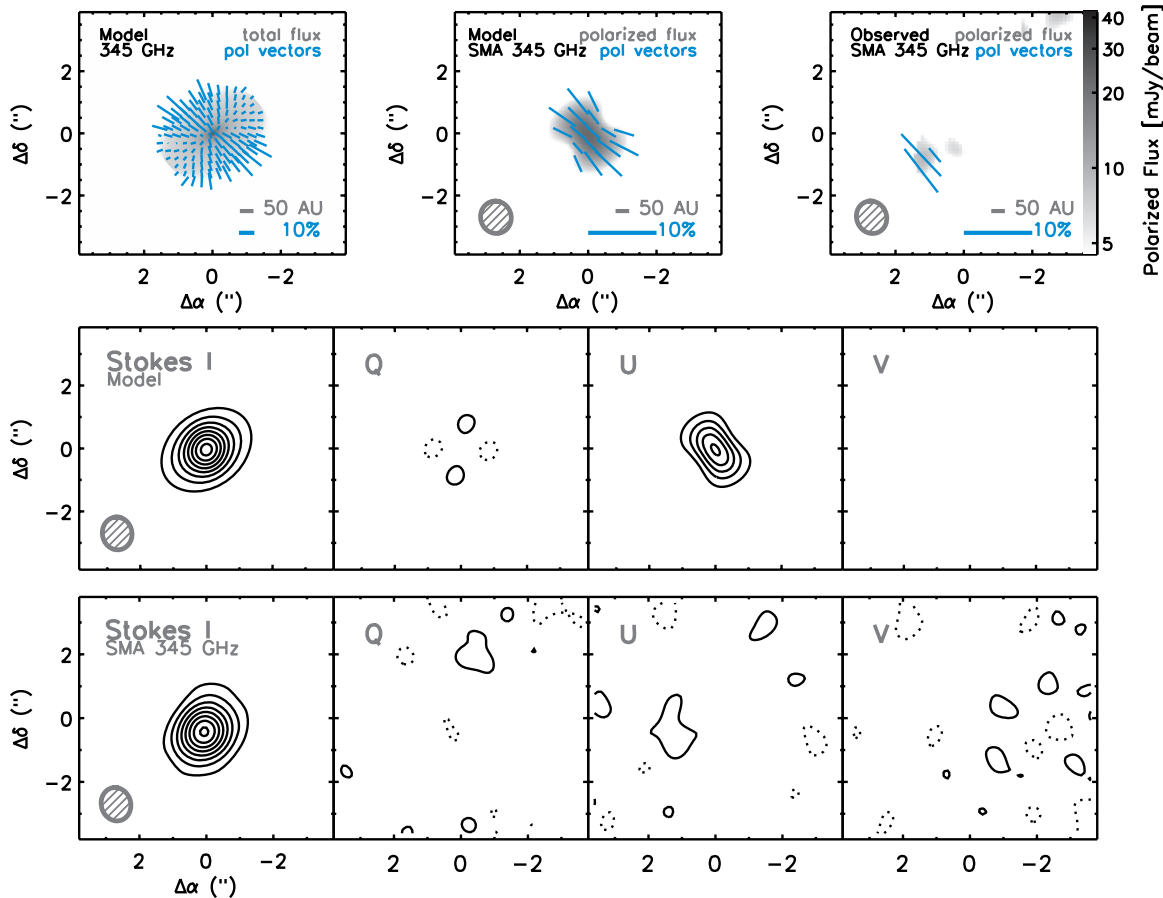
### 3. RESULTS

Figure 1 shows the Stokes  $I$  (unpolarized) visibilities as a function of the distance from the phase center in the  $(u,v)$ -plane, corrected for the projection effects due to the disk inclination as in Lay et al. (1997; for the mathematical definition of the abscissa, see Section 3.3 of Hughes et al. 2008). This is effectively the Fourier transform of the radial brightness distribution of the disk. Both the HD 163296 and TW Hya disks are well resolved with high signal-to-noise ratios.

We detect no polarized emission, in the CO(3-2) line or 880  $\mu$ m continuum, from the HD 163296 or TW Hya disks. The rms values achieved in Stokes  $Q$  and  $U$  for the combined (compact+extended) continuum data are 2.4 mJy beam $^{-1}$  and 2.3 mJy beam $^{-1}$ , respectively, yielding a  $3\sigma$  upper limit in both data sets of 7 mJy beam $^{-1}$ . Given the integrated Stokes  $I$  fluxes of 1.65 Jy and 1.25 Jy for HD 163296 and TW Hya (see Table 1), the Cho & Lazarian (2007) result predictions of 2%–3% polarization at these wavelengths imply  $\sim 30$ –50 mJy of polarized flux. Even if the spatial distribution of polarized flux in the source differs from that of the unpolarized emission,

<sup>10</sup> See <http://cfa-www.harvard.edu/~cqj/mircook.html>.





**Figure 2.** Comparison between the Cho & Lazarian (2007) model and the SMA 340 GHz observations of HD 163296. The top row shows the prediction for the model at full resolution (left), a simulated observation of the model with the SMA (center), and the 2008 SMA observations (right). The gray scale shows either the total flux (left) or the polarized flux (center, right), and the blue vectors indicate the percentage and direction of polarized flux at half-beam intervals. The center and bottom rows compare the model prediction (center) with the observed SMA data (bottom) in each of the four Stokes parameters ( $I$ ,  $Q$ ,  $U$ ,  $V$ , from left to right). Contour levels are the same in both rows, either multiples of 10% of the peak flux ( $0.9 \text{ Jy beam}^{-1}$ ) in Stokes  $I$  or in increments of  $2\sigma$  for  $Q$ ,  $U$ , and  $V$ , where  $\sigma$  is the rms noise of  $2.4 \text{ mJy beam}^{-1}$ . The size and orientation of the synthesized beam are indicated in the lower left of each panel.

(A color version of this figure is available in the online journal.)

we should be able to detect it given that we recover most of the Stokes  $I$  flux. Figures 2 and 3 compare the data with the fiducial model predictions (described in Section 4.1 below). The upper right panel of each figure displays the amount and direction of observed polarized flux for each source, while the bottom row presents contour maps for each of the individual Stokes parameters. The emission in Stokes  $Q$  and  $U$  (linear polarization), as well as in Stokes  $V$  (circular polarization), is consistent with noise. As noted in Section 2, since Stokes  $V$  is calculated as the difference between the measured right and left ( $RR$  and  $LL$ ) circular polarization, the difficulty of calibrating the gains precisely enough to remove the influence of the bright Stokes  $I$  emission raises the rms value in this Stokes parameter relative to Stokes  $Q$  and  $U$ , which are calculated instead from the crossed ( $RL$  and  $LR$ ) polarization states.

We can rule out calibration errors as the reason for the lack of polarized emission for the following three reasons. (1) The point-like test quasars and the similarity of the visibility profiles in Figure 1 with previous observations of these sources (see e.g., Isella et al. 2007; Hughes et al. 2008) illustrate both the success of the atmospheric and instrumental gain calibration and the high sensitivity of the data set. (2) The detection of polarized emission from the test quasars in each of the data sets, with direction consistent between sidebands, demonstrates the success of the

instrumental leakage calibration. Furthermore, (3) several of the nights were shared with other SMA polarization projects, and our solutions for the instrumental leakage between Stokes parameters for the eight quarter-wave plates were effectively identical to those derived by other observers, who successfully detect polarization in their targets.

It is worth comparing the rms noise achieved here with the limiting precision of the current SMA polarimeter. Errors in alignment of the quarter-wave plates introduce instrumental “leakage” between Stokes parameters, allowing some of the flux from Stokes  $I$  to bleed into the linear Stokes parameters. The instrumental leakage correction is quite small ( $\lesssim 3\%$ ) and can, to a large extent, be calibrated by observing a bright point source as it rotates through  $90^\circ$  of parallactic angle. Nevertheless, the uncertainty of this correction under typical observing conditions is  $\sim 0.2\%$ , although this can be reduced to  $\lesssim 0.1\%$  with parallactic angle rotation, provided the source polarization does not vary with time (Marrone 2006). Given the  $2 \text{ mJy beam}^{-1}$  rms noise from our observations compared with the peak Stokes  $I$  fluxes of  $740$  and  $470 \text{ mJy beam}^{-1}$  ( $\sim 0.3\%$ ), our constraints on the polarized flux are approaching the limit of what is achievable with the SMA polarimeter.

It is difficult to directly compare the observations presented here with the Cho & Lazarian (2007) model predictions and

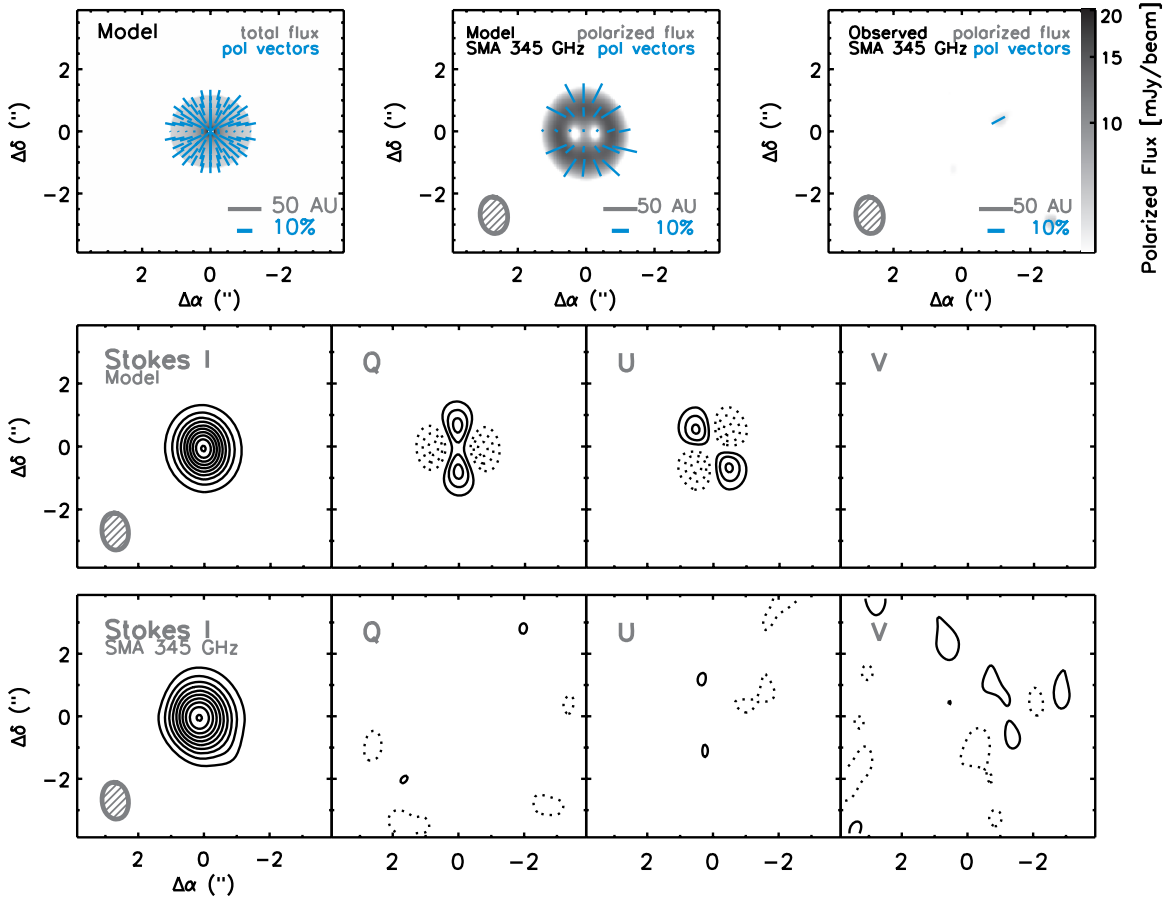


**Figure 3.** Comparison between the Cho & Lazarian (2007) model and the SMA 340 GHz observations of TW Hya. The top row shows the prediction for the model at full resolution (left), a simulated observation of the model with the SMA (center), and the SMA observations (right). The center and bottom rows compare the model prediction (center) with the observed SMA data (bottom) in each of the four Stokes parameters ( $I$ ,  $Q$ ,  $U$ ,  $V$ , from left to right). Contour levels are the same in both rows, either multiples of 10% of the peak flux ( $47 \text{ mJy beam}^{-1}$ ) in Stokes  $I$  or at  $2\sigma$  intervals for  $Q$ ,  $U$ , and  $V$ , where  $\sigma$  is the rms noise of  $2.3 \text{ mJy beam}^{-1}$ . Symbols as in Figure 2.

(A color version of this figure is available in the online journal.)

the Tamura et al. (1999) JCMT result. The 2%–3% polarization factor reported by both sources refers to the integrated emission over the entire spatial extent of the disk. Since the SMA spatially resolves the emission from the disk, the limit on the percent polarization varies with position across the disk. The emission structure is predicted to be quite complicated (Cho & Lazarian 2007), with the percent polarization increasing as a function of distance from the star, so there is no straightforward way to quote a single value for the percent polarization that can be easily compared with the data. By tapering the SMA visibilities with a Gaussian whose FWHM is equal to the diameter of the disk as measured by a truncated power-law model (Hughes et al. 2008), we can simulate an unresolved observation, similar to the JCMT result from Tamura et al. (1999). Using this method, we place a  $3\sigma$  upper limit of 1% on the total polarized flux from both disks. However, such an extreme taper severely downweights the visibilities on the longest baselines, which still have very high signal-to-noise ratios (see Figure 1). This effectively neglects the majority of the data: when all of the spatially resolved data are taken into account, the limits are much more stringent, but they must be compared with the more complicated predictions from the spatially resolved model. Furthermore, decreasing the resolution may be additionally detrimental in the case of more face-on disks like TW Hya: if the magnetic field is perfectly toroidal, then the resulting radial polarization signal will cancel to zero in a large beam, no matter how strong the emission.

To give a rough estimate, the  $\sim 40 \text{ mJy}$  of integrated polarized flux predicted for a 2%–3% polarization fraction resolved into a few beams might predict a peak flux density of  $\sim 20 \text{ mJy beam}^{-1}$ , which is about  $10\sigma$  above the  $\sim 2 \text{ mJy beam}^{-1}$  noise in the data. However, a detailed comparison with the spatially resolved model predictions for each disk can give a more robust result.

The highest signal-to-noise ratio in an image is achieved using natural weighting, which assigns each visibility a weight inversely proportional to its variance. In the case of observations with the SMA polarimeter, the bandwidth and integration time are the same for each integration, so the visibilities are primarily weighted by system temperature. For this reason, we use natural weighting to generate all images presented here. Using the upper limits from the naturally weighted images, it is possible to make comparisons with predictions of the spatially resolved emission generated from the models of Cho & Lazarian (2007). We pursue this avenue of investigation in the following section.

#### 4. ANALYSIS AND DISCUSSION

The constraints on polarized millimeter-wavelength emission from the disks around TW Hya and HD 163296 are inconsistent with previous observational (Tamura et al. 1999) and theoretical (Cho & Lazarian 2007) work that suggested that a polarization fraction of 2%–3% should be common among protoplanetary

disks. The stringent limit on the polarization fraction, when investigated within the context of the Cho & Lazarian (2007) model, can provide clues to the physical conditions within the disk that may be responsible for the suppression of polarized emission relative to the fiducial model prediction. We therefore use the code described in Cho & Lazarian (2007) to generate models of the emission predicted for the TW Hya and HD 163296 disks, using available observational constraints on the disk properties as inputs, and compare these predictions to the upper limits from the SMA observations (Section 4.1). We then identify parameters that are not well constrained by existing observations, and which have the greatest effect on the polarized emission rather than unpolarized Stokes  $I$  emission. We vary these parameters and investigate their effects on the predicted polarized submillimeter emission. We infer the range of values over which the predictions are consistent with the observations as well as the interactions between parameters in the context of the models (Section 4.2). Finally, we investigate other effects *not* implemented in these models that may contribute to the suppression of polarized disk emission, and estimate the magnitude of their contribution (Section 4.3).

#### 4.1. Initial Models

The Cho & Lazarian (2007) predictions employ a two-layered Chiang et al. (2001) model of the density and temperature structure of a protoplanetary disk, including a surface layer with hot, small dust grains, and an interior with cooler, larger grains. Within this model, the elongated dust grains are allowed to align via the radiative torque mechanism with a perfectly toroidal magnetic field threading the disk. The dust grains are assigned a size distribution described by a power law  $dN \propto r^{-q_{\text{grain}}} dr$ , where  $N$  is the number of grains of size  $r$ , and  $q_{\text{grain}}$  is initially taken to be 3.5 (Mathis et al. 1977). The grains are also assigned a degree of elongation given by the ratio of long-to-short axis cross sections,  $C_{\perp}/C_{\parallel}$ , where  $C_{\perp}$  and  $C_{\parallel}$  are the polarization cross sections for the electric field perpendicular and parallel to the grain symmetry axis, respectively. The grain size is defined as  $r$ , such that  $C_{\perp} = (1 + \alpha)\pi r^2$  and  $C_{\parallel} = (1 - \alpha)\pi r^2$ , where  $\alpha$  parameterizes the degree of elongation. The ratio of the major and minor axes of the grain is then given by  $a/b = \sqrt{(1 + \alpha)/(1 - \alpha)}$ . The grain shape is assumed to be oblate as in Cho & Lazarian (2007), consistent with observational evidence described in Hildebrand & Dragoon (1995). The initial 2%–3% polarization estimates are based on the parameters for the “typical” T Tauri disk investigated in Chiang et al. (2001).

In order to generate a model prediction that can be compared with the upper limits from the SMA observations, we adjust these parameters to reflect the best available information about the grain properties and density structures in the disks around HD 163296 and TW Hya. The initial model inputs, with references, are summarized in Table 2. We use temperature and surface density power-law indices and outer radii derived from previous SMA 345 GHz continuum observations (Hughes et al. 2008). The temperatures are calculated from the stellar temperature and gas and dust densities and opacities as in Chiang et al. (2001), while the surface density is adjusted to best reproduce the observed 880  $\mu\text{m}$  continuum flux. The temperatures and surface densities calculated here are consistent with previously determined values (e.g., Isella et al. 2007; Hughes et al. 2008) to within a factor of 2. Variations can be attributed to differences in the vertical temperature structure and dust grain opacities assumed in the models. While these disk structure models do not precisely reproduce the observed brightness profile, they

**Table 2**  
Initial Model Parameters

Parameter <sup>a</sup>	HD 163296		TW Hya	
	Value	Ref.	Value	Ref.
$T_*$ (K)	9330	1	4000	2
$R_*$ ( $R_{\odot}$ )	2.1	1	1.0	2
$M_*$ ( $M_{\odot}$ )	2.3	1	0.6	2
$p$	0.8	3	1.0	3
$a_{\text{inner}}$ (AU)	0.45	4	4.0	5, 6
$a_0$ (AU)	200	3	60	3
$r_{\text{max},i}$ ( $\mu\text{m}$ )	$10^3$	4	$10^4$	7
$i$	$46^{\circ}$	4	$7^{\circ}$	8
$d$ (pc)	122	1	51	9, 10
$\Sigma_0$ ( $\text{g cm}^{-2}$ )	130	...	170	...

#### Notes.

<sup>a</sup> Symbols as in Chiang et al. (2001):  $T_*$ ,  $R_*$ , and  $M_*$  are stellar temperature, radius, and mass, respectively;  $p$  and  $\Sigma_0$  describe the surface density profile  $\Sigma(R) = \Sigma_0(R/1\text{AU})^{-p}$ ,  $a_0$  is the outer disk radius, and  $r_{\text{max},i}$  is the maximum dust grain size in the disk interior. Additionally, we define  $a_{\text{inner}}$  (disk inner radius),  $i$  (inclination), and  $d$  (distance). All parameters not listed here are equal to the fiducial input parameters from Chiang et al. (2001).

**References.** (1) van den Ancker et al. 1998; (2) Webb et al. 1999; (3) Hughes et al. 2008; (4) Isella et al. 2007; (5) Calvet et al. 2002; (6) Hughes et al. 2007; (7) Wilner et al. 2005; (8) Qi et al. 2004; (9) Mamajek 2005; (10) Hoff et al. 1998.

represent a reasonable approximation within which the parameters determining the polarization properties of interest can be investigated.

We use the model routines to generate  $400 \times 600$  pixel sky-projected images (i.e., with 6 and 8 mas pixels for TW Hya and HD 163296, respectively, significantly more finely spatially sampled than the data) giving the total continuum flux, percent polarization, and orientation of polarized emission at each position across the disk. The full-resolution model is shown in the upper left panel of Figures 2 and 3, although the lines indicating orientation have been vector-averaged in bins of several pixels for clarity of display. We then use the MIRIAD task `uvmodel` to sample the image with the same spatial frequencies as the SMA data. We invert the visibilities and image with natural weighting to create a simulated SMA observation of the disk model, shown in the top center panel of Figures 2 and 3. We also create simulated images in each of the four Stokes parameters (center row), since the Stokes parameter images are most directly comparable to the upper limits set by the observations. The model images show the distinctive quadrupolar pattern in Stokes  $Q$  and  $U$  predicted by the model for a toroidal magnetic field geometry, due to the radial orientation of the polarization vectors. The intermediate inclination of HD 163296 creates an hourglass-shaped bright region along the disk minor axis, where the synthesized beam picks up emission from the highly polarized regions along the front and back of the outer disk, concentrated toward the disk center by the viewing geometry. This predicted morphology echoes the alignment of polarization vectors with the minor axes of the disk observed by Tamura et al. (1999). With predicted peak Stokes  $Q$  and  $U$  fluxes of 23 and 16 mJy beam $^{-1}$ , these initial models of polarized emission are ruled out at the  $10\sigma$  and  $7\sigma$  level for HD 163296 and TW Hya, respectively, by the SMA upper limits.

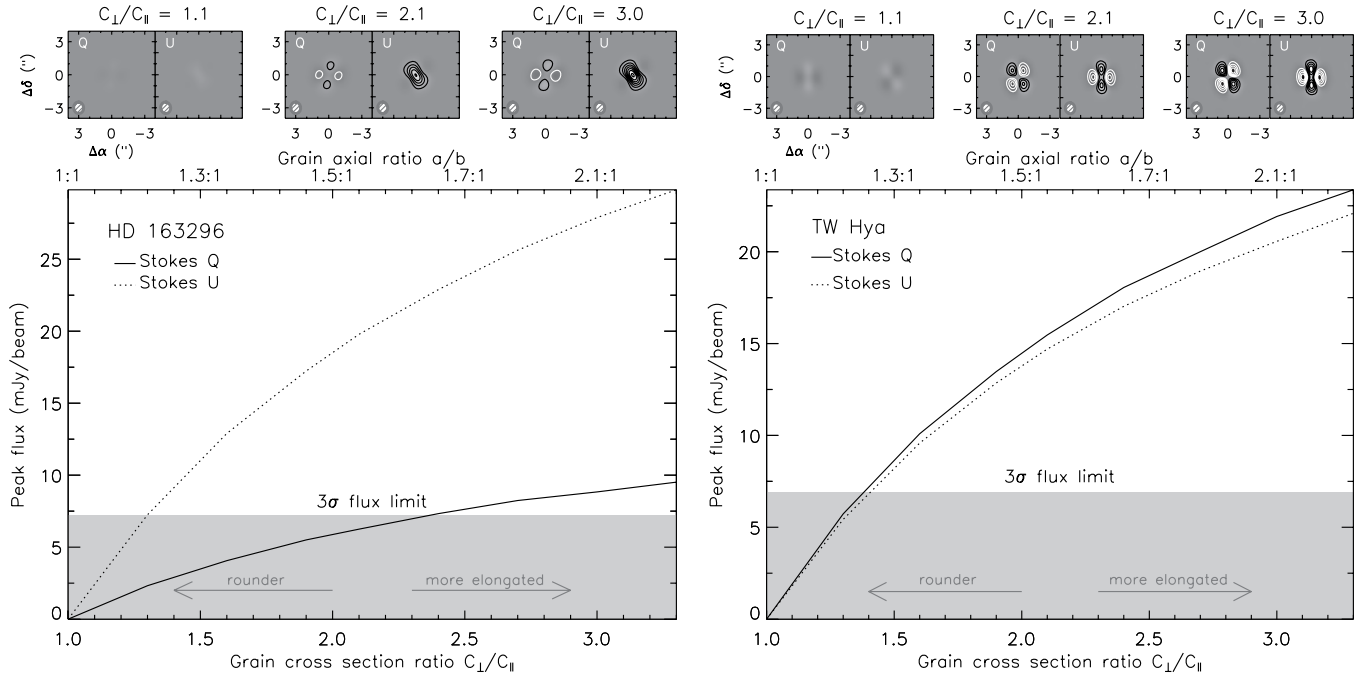


**Figure 4.** Peak continuum flux in Stokes  $Q$  and  $U$  as a function of dust grain cross section ratio for HD 163296 (left) and TW Hya (right). The top row shows the resolved emission in Stokes  $Q$  and  $U$  predicted for three values of the dust grain cross section ratio, sampled at the same spatial frequencies as the data. The gray scale indicates the intensity of emission relative to the peak flux of the data when the grain cross section ratio equals 3, with white indicating positive emission and black indicating negative emission. Contours are [2, 4, 6,...] times the rms noise (2.4 mJy for HD 163296 and 2.3 mJy for TW Hya) with positive contours in black and negative contours in white. The plots below give the peak flux in the synthesized beam predicted by the models as a function of the grain cross section ratio. Stokes  $Q$  is plotted as a solid line while Stokes  $U$  is a dotted line. The  $3\sigma$  upper limit on the peak flux from the SMA observations is indicated by the gray region of the plot. The y-axis along the upper edge of the plot gives the dust grain axial ratio. All images and peak flux values assume natural weighting to minimize noise.

#### 4.2. Parameter Exploration

With the fiducial model prediction ruled out at high confidence, we turn to an exploration of the input parameter space to provide information about the conditions in the disk that might be responsible for the suppression of polarized emission. We first identify several parameters that most strongly affect the polarization properties of the disk, without significant impact on the Stokes  $I$  emission. In the Cho & Lazarian (2007) model, the radiative torque mechanism that spins up elongated dust grains along magnetic field lines is impeded primarily by gas drag in regions of high density. Since we normalize the surface density to reproduce the  $880\ \mu\text{m}$  flux (for the assumed opacities and derived temperatures), we cannot vary this quantity. However, the degree of elongation of the dust grains, the threshold set within the model for grain alignment, and the dust grain size distribution are all important factors that affect the polarization properties of the disk rather than the Stokes  $I$  emission. These parameters are discussed in greater detail in the following sections.

##### 4.2.1. Grain Elongation

The elongation of the dust grains is important both for the radiative torque and because the differing cross sections parallel and perpendicular to the magnetic field allow the grain to emit polarized continuum emission at millimeter wavelengths. The fiducial model assumes a long-to-short axis cross section ratio  $C_{\perp}/C_{\parallel} = 2.1$ , corresponding to an axial ratio of 1.5:1 for oblate dust grains (for the relationship between cross section and axial ratios for different grain geometries, see e.g., Padoan et al. 2001). Varying this ratio determines the radial extent of the disk over which the dust grains are aligned with the magnetic field, as well as how much polarized light is emitted from the disk: it

effectively changes the efficiency of grain alignment and the emission cross section of the grains.

In order to obtain a quantitative description of the effect of grain elongation on the predicted intensity of polarized emission from the disk, we generate a series of models with different cross section ratios as described in Cho & Lazarian (2007) with initial parameters listed in Table 2. We then sample the model images with the SMA spatial frequencies, as described in Section 4.1 above, and compare the peak flux in Stokes  $Q$  and  $U$  with the  $3\sigma$  upper limit from the SMA observations. Figure 4 plots the peak flux in the Stokes  $Q$  and  $U$  model images as a function of the dust grain cross section ratio. For comparison, the shaded area marks the region of parameter space consistent with the  $3\sigma$  upper limits from the SMA observations. The series of panels across the top of the plot show the model images in Stokes  $Q$  and  $U$ , sampled with the SMA spatial frequencies, for three representative values of the dust grain cross section ratio. From these maps, it is clear that the dust grain elongation acts primarily as a scaling factor for observations at this resolution: the emission morphology does not change, but simply becomes stronger or weaker as the dust grains become more or less elongated. From the HD 163296 plot on the left and the TW Hya plot on the right, we can see that if the dust grain elongation were the only factor suppressing polarized emission from the disk, the grains would have to be quite round, with  $C_{\perp}/C_{\parallel} \lesssim 1.2\text{--}1.3$ .

##### 4.2.2. Grain Alignment Criterion

Another model input that is important for the polarization properties of the disk is the value at which the threshold for grain alignment via the radiative torque is set. In order to determine whether or not the dust grains are aligned with the magnetic field in a particular region of the disk, a comparison is made between



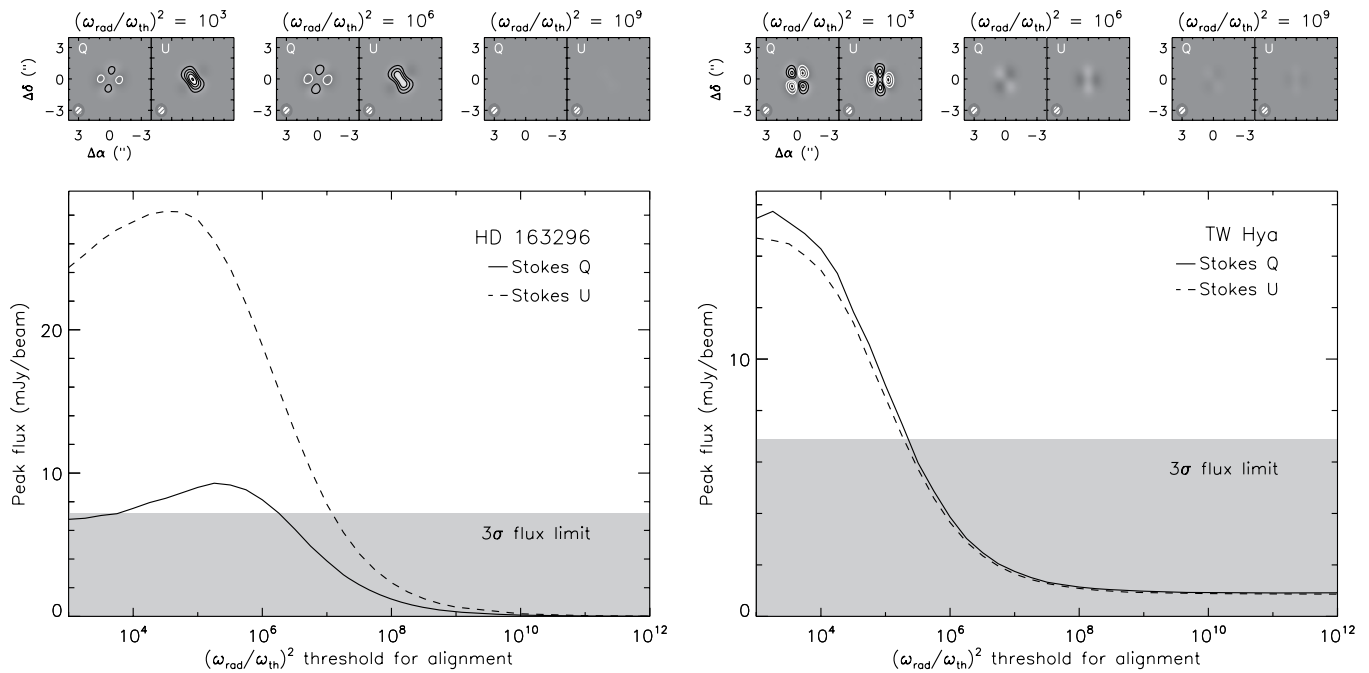


**Figure 5.** Peak continuum flux in Stokes  $Q$  and  $U$  as a function of the threshold for grain alignment (see Section 4.2 in the text) for HD 163296 (left) and TW Hya (right). The top row shows the resolved emission in Stokes  $Q$  and  $U$  predicted for three values of the alignment threshold, sampled at the same spatial frequencies as the data. The gray scale indicates the intensity of emission relative to the peak flux of the data when the alignment threshold equals  $10^3$ , with white indicating positive emission and black indicating negative emission. Contours are  $[2, 4, 6, \dots]$  times the rms noise (2.4 mJy for HD 163296 and 2.3 mJy for TW Hya) with positive contours in black and negative contours in white. The plots below give the peak flux in the synthesized beam predicted by the models as a function of the alignment threshold. Stokes  $Q$  is plotted as a solid line while Stokes  $U$  is a dotted line. The  $3\sigma$  upper limit on the peak flux from the SMA observations is indicated by the gray region of the plot. The y-axis along the upper edge of the plot gives the dust grain axial ratio. All images and peak flux values assume natural weighting to minimize noise.

the rotational kinetic energy imparted by the radiative torque and that imparted by random collisions with gas particles in the disk. A useful parameterization is  $(\omega_{\text{rad}}/\omega_{\text{th}})^2$ , where  $\omega_{\text{rad}}$  and  $\omega_{\text{th}}$  are the angular velocities of the grains due to radiative torques and thermal collisions, respectively. The radiative torques act to align grains with the magnetic field, while gas drag inhibits alignment and causes grains to point in random directions: the ratio  $(\omega_{\text{rad}}/\omega_{\text{th}})^2$  therefore serves as a measurement of the effectiveness of the radiative torque in aligning the grains with the magnetic field. This ratio will generally be highest, and the grains most aligned, in the outer disk where the gas density is low. We therefore expect grains to be aligned in the outer disk, and oriented randomly in the inner disk. Since the value of  $(\omega_{\text{rad}}/\omega_{\text{th}})^2$  varies with the radial distance from the star, the chosen threshold value for alignment effectively varies the radius at which grains become aligned with the disk magnetic field. The threshold is initially set so that grains are assumed to be aligned in regions of the disk where the kinetic energy imparted by the radiative torque is  $10^3$  times greater than that imparted by thermal collisions. We vary this threshold in order to study its effects on the polarization properties of the disk.

Figure 5 shows the peak flux predicted for Stokes  $Q$  and  $U$  as a function of the grain alignment threshold  $(\omega_{\text{rad}}/\omega_{\text{th}})^2$ , compared with the  $3\sigma$  upper limit from the SMA observations for HD 163296 (left) and TW Hya (right). It is clear that for both disks, the threshold would have to be set many orders of magnitude higher than the conservative initial value in order for the alignment to be weak enough to account for the lack of a polarization signal. Indeed, in order for this to be the primary mechanism suppressing the disk polarization, the threshold would need to be raised until alignment is permitted to occur only when the rotational kinetic energy imparted by the radiative

torque is at least 5–7 orders of magnitude greater than that of gas grain collisions. This is most likely an unrealistically stringent constraint.

It should be noted here that the approach to alignment in Cho & Lazarian (2007) requires revisions to account for recent advances in the quantitative theory of grain alignment. First of all, in the calculations of the ratio  $(\omega_{\text{rad}}/\omega_{\text{th}})$ , the simplifying assumption is made that the radiation seen by each grain is coming from a point source. In fact, the bulk of the radiation field originates as reprocessed starlight from neighboring regions of the disk, so although there should be an overall radial gradient, it is better approximated by multipoles rather than a purely unidirectional signal. When the effects of this radiation structure are accounted for, the ratio  $(\omega_{\text{rad}}/\omega_{\text{th}})$  can decrease by up to a factor of 10 (Hoang & Lazarian 2009, Figure 17). An additional decrease by another factor of  $\sim 10$  may come from the fact that the overall direction of anisotropy is perpendicular to the assumed toroidal magnetic field in the disk (Hoang & Lazarian 2009, Figure 17). This effect may be mitigated somewhat in a clumpy disk, where local anisotropies will not necessarily be radially oriented and may even be aligned with the magnetic field. Taking both effects into account and squaring the ratio demonstrates that the kinetic energy of the grains in their maximal state of rotation may be up to four orders of magnitude less than is assumed using ad hoc assumptions in the spirit of the old understanding of radiative torque alignment. An additional decrease comes from the fact that an appreciable portion of grains may be aligned in the so-called “zero- $J$ ” alignment point (Lazarian & Hoang 2007). Grains in this point are not perfectly aligned as assumed in Cho & Lazarian (2007), but instead will wobble, reducing the degree of alignment to only  $\sim 20\%$  (see Hoang & Lazarian 2008). In addition, while interstellar grains

are always aligned with long axes perpendicular to the magnetic field, larger grains in circumstellar disks may not have efficient internal relaxation and can be occasionally aligned with long axes parallel to the magnetic field (Hoang & Lazarian 2009). These factors can significantly decrease the observed degree of polarization expected from the circumstellar disks compared to the Cho & Lazarian (2007) estimate, making the predictions roughly comparable (to within an order of magnitude or so) to the SMA upper limits.

#### 4.2.3. Grain Size Distribution

Cho & Lazarian (2007) emphasize the importance of the grain size distribution in determining the observed polarization properties of circumstellar disks. We fix the minimum grain size at  $r_{\min} = 0.01 \mu\text{m}$  as in Cho & Lazarian (2007) and Chiang et al. (2001). Although growth to larger sizes may have occurred, the minimum grain size affects the millimeter-wavelength polarization properties in the context of the model only through the normalization of the total mass: increasing the minimum grain size to  $1 \mu\text{m}$  (required to reproduce the  $10 \mu\text{m}$  silicate feature from the inner disk; see e.g., Calvet et al. 2002) changes the predicted polarization by less than 0.1%, since it does not bring the density above the threshold value necessary to suppress grain alignment in the outer disk. Two aspects of the grain size distribution that can be varied in the context of the model are the maximum grain size  $r_{\max}$  and the power-law index  $q_{\text{grain}}$ , where the grain size number density goes as  $dN \propto r^{-q_{\text{grain}}} da$ .

Observational evidence points to grain growth up to at least 1 mm in the HD 163296 disk (Isella et al. 2007) and 1 cm in the TW Hya disk (Wilner et al. 2005), without ruling out the possibility that grains have grown to even larger sizes (perhaps even planetary dimensions in the case of TW Hya; see Calvet et al. 2002; Hughes et al. 2007). Since the surface density is chosen to maintain consistency with the observed  $880 \mu\text{m}$  flux in Stokes  $I$ , the number density of particles with sizes near  $880 \mu\text{m}$ , which dominate the  $880 \mu\text{m}$  flux, remains roughly constant regardless of the maximum grain size in the distribution. Thus, the effect of raising the maximum grain size in the distribution is primarily to introduce “invisible” grains at sizes larger than 1 mm or 1 cm, which has no effect on the observable polarization properties (cf. Figure 7 in Cho & Lazarian 2007). However, adding mass at the large-grain end of the size distribution while keeping constant the mass in small grains has the effect of raising the total surface density of the disk. This is unrealistic for all but a small increase in maximum grain size, as the disk quickly becomes Toomre unstable, and gravitational collapse or deviations from Keplerian rotation should rapidly become observable. While this is most likely an artifact of the assumed grain size distribution, it suggests that within the context of the model, grain growth is unlikely to be the mechanism suppressing the emission of polarized radiation.

The power-law index  $q_{\text{grain}}$  controlling the relative population of large and small grains in the disk is somewhat more promising. In general, the polarized emission observed at a particular wavelength will tend to originate primarily from dust grains smaller than the wavelength, while the unpolarized emission will be dominated by grains of roughly the same size as the wavelength. Because dust grains of size  $\sim 880 \mu\text{m}$  are within the geometric optics regime ( $2\pi r/\lambda > 1$ , where  $\lambda$  is the wavelength of observation,  $880 \mu\text{m}$ ), they do not contribute to the polarized emission predicted by the models. Most of the Stokes  $Q$  and  $U$  emission at these wavelengths originates

from dust grains with sizes less than  $\lambda/2\pi \approx 100 \mu\text{m}$  (Cho & Lazarian 2007), while most of the Stokes  $I$  emission originates from grains with sizes similar to the wavelength of observation. The relative number of 100 and  $880 \mu\text{m}$  grains in the disk, determined by  $q_{\text{grain}}$ , therefore plays a role in determining the amount of polarized emission observed. However, since the differences in grain sizes are not large, the power-law index must change substantially before the effect on the polarization properties becomes appreciable. Varying  $q_{\text{grain}}$  from 3.5 to 2 changes the peak linearly polarized flux in the model by only 20%. Therefore, when comparing the SMA limits with the model predictions, the dust grain size distribution has relatively little impact on the predicted polarization properties of the disks.

#### 4.2.4. Interactions Between the Parameters

The analysis so far has explored individual model parameters as though they were fully independent, determining the range of values permitted by the SMA upper limit for each parameter separately. However, it is useful to understand how the parameters relate to one another in determining the polarization properties of the disk. Here we investigate relationships between pairs of the parameters considered above.

We first study the relationship between dust grain elongation and the grain alignment threshold. As discussed in Section 2.3 of Cho & Lazarian (2007), the rotation rate of dust grains due to the radiative torque is a function of the peak wavelength of the radiation field and the dust grain size, with no explicit dependence on the grain axial ratio. As described in Dolginov & Mitrofanov (1976), spin-up by the radiative torque mechanism is caused by the irregular shape of the grain, which gives it differing cross sections to left and right circular polarizations; elongation does not necessarily favor either polarization basis. This is reflected in the table of timescales relevant for grain alignment in Lazarian (2007): neither the radiative precession time nor the gas damping time depends on the grain axial ratio. The primary effect of the grain elongation in alignment is to decrease the Larmor precession time, which causes the spinning grains to align their major axes more quickly with the magnetic field lines (or, alternatively, decreases the critical magnetic field strength in a given region of the disk; see Section 4.3 below). We therefore do not expect much, if any, dependence between these variables. In order to test this expectation, we vary the dust grain cross section ratio and the grain alignment threshold for the HD 163296 disk. The model prediction of peak flux in Stokes  $U$  (which provides the most stringent limits when compared to the SMA data) is shown in Figure 6. The shaded gray region of the plot represents the parameter space within which the model prediction is less than the  $3\sigma$  upper limit given by the SMA data, i.e., combinations of parameters consistent with the observational results. The contours show the predicted peak flux of the model in Stokes  $U$  for each combination of parameters: model predictions with greater polarized intensity are more strongly inconsistent with the observational limits. Because of the assumption in the models that grains meeting the alignment criterion will become aligned with 100% efficiency, grain alignment and elongation are evidently only weakly coupled.

Another potentially important relationship is that between the grain size distribution and grain elongation. Little is known about the relationship between these variables, since both are notoriously difficult to constrain observationally. Nevertheless, if grains grow simply by accumulating material evenly over their surface then they may naturally become more spherical as

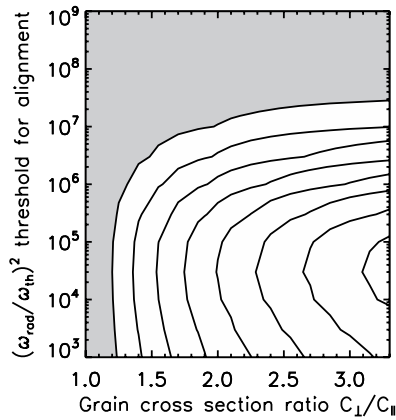


**Figure 6.** Detectability of Stokes  $U$  continuum emission from the HD 163296 disk as a function of the dust grain cross section ratio (Section 4.2.1) and the threshold for dust grain alignment (Section 4.2.2). The gray regions of the plot represent portions of the parameter space that would be undetectable given the  $3\sigma$  upper limit from the SMA observations, while contours show the peak flux of the model for each set of parameters, beginning at the  $3\sigma$  level (7.2 mJy) and increasing by intervals of  $2\sigma$  (4.8 mJy). The two parameters are only weakly degenerate.

they become larger. Spherical grains emit less strongly polarized radiation than more elongated grains, so it might be expected that grain growth can suppress the emission of polarized light, even in cases where the alignment mechanisms are quite efficient (as expected for large grains, e.g., Cho & Lazarian 2005). Indeed, a corresponding inverse relationship between grain size and polarization fraction has been observed in molecular clouds (e.g., Vrba et al. 1993). Given the observed growth to millimeter and even centimeter sizes within the disks around HD 163296 and TW Hya (Isella et al. 2007; Wilner et al. 2005), and the large ( $\sim 100 \mu\text{m}$ ) sizes of the grains responsible for emitting most of the polarized radiation (see Section 4.2.3), it is perhaps plausible that the grains in these disks should have cross section ratios consistent with the values of 1.2–1.3 constrained in Section 4.2.1 above. We know that this cannot be true everywhere in the interstellar medium (ISM): polarization at  $850 \mu\text{m}$  is observed in star-forming regions at much earlier stages (e.g., Girart et al. 2006), and far-infrared polarimetry indicates that grains with axial ratios  $a/b$  between 1.1 and 3 are common at sizes of tens of microns in molecular clouds (Hildebrand & Dragovan 1995). However, a tendency toward spherical grains in T Tauri disks, even just at the low end of the distribution inferred by Hildebrand & Dragovan (1995), should be able to suppress the emission of polarized radiation from the disk enough to bring the models within the range of the observational constraints.

We can test the plausibility of this degree of elongation by modifying the discussion of grain growth based on turbulent coagulation in Vrba et al. (1993). If we assume that the grains in T Tauri disks originate exclusively from small, highly elongated grains in the ISM, e.g., with initial major axis  $a_i = 0.1 \mu\text{m}$  and axial ratio  $a_i/b_i = 2$  (Aannestad & Purcell 1973; Hildebrand & Dragovan 1995), then we can estimate how the axial ratio changes with the grain size. Neglecting asymmetric effects like collisional destruction, the grain size might be expected to grow roughly evenly in all directions with the number of grain–grain collisions,  $N$ , in such a way that the final grain size is simply  $a_f = a_i N^{1/3}$ . The change in any dimension of the grain,  $\delta$ , is then given by  $\delta = a_i N^{1/3} - a_i$ , yielding a final minor axis size of  $b_f = b_i + \delta$ , or  $a_f/b_f = a_f/(a_f - a_i + b_i)$ . If  $a_i = 0.1 \mu\text{m}$  and  $a_f = 100 \mu\text{m}$ , then  $a_f/b_f = 1.001$ , significantly

more round than the upper limit set by the SMA data. The timescale needed for grain growth to these (up to meter) sizes is of order  $10^5$  yr at a distance of 50 AU from the central star (see e.g., Weidenschilling 1988; Dullemond & Dominik 2005). This calculation is highly simplified and neglects complications like the evolution of conditions within the disk, shaping by grain–grain collisions (e.g., Dullemond & Dominik 2005), and the complexity of the grain size distribution. Yet the extremely spherical grains produced on relatively short timescales in this oversimplified scenario represent a lower limit to the grain elongation that perhaps suggests a scenario by which grains might have grown into shapes that are nearly spherical enough (with axial ratios of 1.2 rather than 1.001) to plausibly account for the suppression of polarized emission.

### 4.3. Other Effects

In the previous section, we investigated the effects of those parameters considered in the Cho & Lazarian (2007) model. However, there are additional effects that may also play a role in suppressing polarized emission from the disk relative to the fiducial 2%–3% prediction. Among these are the magnetic field strength, the geometric regularity of the magnetic field, and polarization due to scattering.

#### 4.3.1. Magnetic Field Strength

The magnetic field strength plays a role in determining whether or not grains can become aligned via the radiative torque. If the magnetic field is above some critical strength, grains will become aligned provided that the radiative torque can generate more rotational kinetic energy than thermal collisions. At low magnetic field strengths, grains are not expected to align with the magnetic field at all. The critical magnetic field strength for alignment may be estimated by comparing the Larmor precession time  $t_L$  with the gas damping time  $t_{\text{gas}}$ . Following Lazarian (2007) and using fiducial values for the magnetic susceptibility and dust grain density, alignment is possible when  $t_L < t_{\text{gas}}$ , or

$$B > 4.1 \times 10^{-5} \frac{rnT_d T_g^{1/2}}{s^2}, \quad (1)$$

where  $B$  is the magnetic field strength in units of  $\mu\text{G}$ ,  $r$  is the grain size in cm,  $n$  is the gas density in units of  $\text{cm}^{-3}$ ,  $T_d$  is the dust temperature in K,  $T_g$  is the gas temperature in units of K, and  $s$  is the ratio of minor to major dust grain axes. Using the power-law models of density and temperature derived in Hughes et al. (2008), it is possible to estimate these quantities for the regions of the outer disk probed by the SMA data. Taking the values at disk radii equivalent to the spatial resolution of the data ( $\sim 1''0$ , or 50 and 120 AU for TW Hya and HD 163296, respectively), and assuming equivalent gas and dust temperatures, we derive densities of several times  $10^8 \text{ cm}^{-3}$  and temperatures of  $\sim 40$ – $50$  K. For the  $10$ – $100 \mu\text{m}$  grains contributing most of the polarized emission in the models, the critical magnetic field strength is of order  $10$ – $100$  mG.

This strength matches reasonably well with theoretical expectations. Shu et al. (2007) developed a model of steady-state magnetized accretion disks that predict magnetic field strengths of order  $10$ – $100$  mG on the spatial scales probed by the data. Wardle (2007) pointed out that Zeeman splitting of OH in molecular cloud cores and masers in star-forming regions place a lower limit of  $\sim 10$  mG on the magnetic field strength, which will likely be amplified by compression and shear during the



process of collapse that forms the central star and disk. It should also be noted that the value quoted above should be taken as a lower limit, since superparamagnetic inclusions would significantly decrease the required magnetic field strength for alignment (Lazarian & Hoang 2008). The critical magnetic field strength required to align grains within the conditions of the model is therefore reasonable compared to theoretical expectations. We do not expect that the lack of polarized emission is due to extremely low magnetic field strengths.

#### 4.3.2. Geometric Regularity of the Magnetic Field

The assumption that the field is toroidal arises from the supposition that the rotational motion of the disk has affected the magnetic field geometry. Yet for this to occur, the ionization fraction must be large enough that disk material and magnetic fields can interact. However, this also implies that turbulent motions within the disk (perhaps even of magnetic origin) may tangle the magnetic fields locally, adding a random component to the ordered toroidal magnetic field. It is extremely difficult to estimate the magnitude of such an effect without knowing both the ionization fraction and the magnitude of turbulence as a function of the position in the disk. Lee & Draine (1985) discuss the effect of a random magnetic field component on the strength of the observed polarization signature, and note that the strength of polarized emission will be reduced by a factor  $F = 3/2(\langle \cos^2 \theta \rangle - 1/3)$ , where  $\theta$  is the angle between the local magnetic field and the direction of the ordered global magnetic field. This quantity varies from one (perfectly ordered field;  $\langle \cos^2 \theta \rangle = 1$ ) to zero (perfectly random field;  $\langle \cos^2 \theta \rangle = 1/3$ ), but the exact value depends on the details of the local magnetic field geometry. If magnetic field tangling were the sole factor responsible for the difference between the fiducial modeling prediction and the SMA upper limits, we would constrain  $F$  to be less than  $\sim 0.1$  for the case of HD 163296, implying  $\langle \cos^2 \theta \rangle < 0.4$ , which indicates an almost completely random magnetic field structure.

It should also be noted that grain alignment efficiency would play a similar role, quantified in exactly the same way as  $F$  above, with  $\theta$  indicating the angle between the long axis of the grain rather than the angle between the local and global magnetic fields (Greenberg 1968; Lee & Draine 1985). The Cho & Lazarian (2007) code assumes 100% efficient alignment in regions that meet the grain alignment criterion (Section 4.2.2). In order to account fully for the suppression of polarized emission relative to the fiducial model, the alignment efficiency would have to be quite low, less than 10% in the case of HD 163296.

The tentative single-dish detections appear to indicate a toroidal magnetic field geometry for the disks around DG Tau and GM Aur, consistent with observations indicating a dominant toroidal component to the magnetic field in the flattened structures around young stellar objects at earlier evolutionary stages (see Wright 2007, and references therein). However, it is also possible that the field could be poloidal: as discussed e.g., in Shu et al. (2007), a magnetic field gathered from the interstellar medium that threads vertically through the disk might be expected to remain poloidal in geometry as it interacts with disk material. While the SMA limits are unable to constrain the magnetic field geometry, a poloidal geometry might be expected to reduce the expected polarization signature particularly for the case of a face-on viewing geometry as in the case of the TW Hya disk. The effects of a poloidal geometry for a disk viewed at intermediate inclination, like HD 163296, are less clear and are not investigated in the context of the Cho &

Lazarian (2007) models, although it is plausible that the strength of polarized emission from a toroidal or poloidal field would be comparable.

#### 4.3.3. Scattering

Cho & Lazarian (2007) argue that scattering contributes significantly less than thermal emission to the polarized flux at millimeter wavelengths in the disk. In order to estimate the relative contribution of scattering and emission at a range of radii throughout the disk, they compare the product  $J_\lambda \kappa_{\text{scatt}}$ , where  $J_\lambda$  is the mean radiation field, and  $\kappa_{\text{scatt}}$  is the mass scattering coefficient, to the product  $B_\lambda \kappa_{\text{abs}}$ , where  $B_\lambda$  is the intensity of blackbody radiation in the region of interest, and  $\kappa_{\text{abs}}$  is the mass absorption coefficient. They show that in the outer disk, where  $R \gtrsim 10$  AU, the ratio of these products falls below 1 (and ultimately below 0.5), indicating that emission is dominant over scattering in the outer disk.

It is of interest, however, that pure scattering of light from a central source off of large grains in the outer disk should produce a polarization signal precisely orthogonal to that expected for elongated grains aligned with a toroidal magnetic field. While the radiation field at  $850 \mu\text{m}$  is dominated by the local conditions rather than a central source, as discussed in Section 4.2.2 there will be an overall radially anisotropic component of the radiation field that might be expected to produce a weaker, but still orthogonal on average, scattering signal. The contribution from scattering would therefore generally act to cancel the expected polarization signal from emission. An estimate of the magnitude of the scattered light signal compared with the predicted strength of polarized emission is beyond the scope of this paper, but we note that for scattering to be the dominant mechanism suppressing the expected polarization signal, the intensity of polarized emission arising from scattering and emission would have to be precisely equivalent, to within 10%–15%, in both disks. Furthermore, since the scattering and emission have different wavelength dependences, the coincidental canceling of the emission signal would only occur at the wavelength of observation. In the absence of any expectation that these quantities should be related, this seems an unlikely coincidence.

## 5. SUMMARY AND CONCLUSIONS

Despite the expectation of a 2%–3% polarization fraction in circumstellar disks based on previous observational and theoretical work (Tamura et al. 1999; Cho & Lazarian 2007), the SMA polarimeter observations presented here show no polarization from the disks around two nearby stars. With these observations we place a  $3\sigma$  upper limit on the integrated polarization fraction of less than 1% and rule out the fiducial Cho & Lazarian (2007) models at the  $\sim 10\sigma$  level. These represent the most stringent limits to date on the magnitude of submillimeter polarized emission from circumstellar disks. We are therefore left with the question of which model assumptions are unrealistic enough to account for an approximately order-of-magnitude (at minimum) overprediction of the polarization signal from these disks.

Among the model parameters and additional effects considered in Section 4, several seem unlikely as the source of the suppression of polarized emission. The critical magnetic field strength expected for alignment seems reasonable relative to theoretical expectations and observations. An almost completely random magnetic field with no dominant toroidal (or poloidal) component would also be surprising, although a poloidal field



geometry would be expected to significantly weaken the polarized emission arising from a face-on disk like TW Hya. Scattering is expected to be weak, but it should produce a polarization signature perpendicular to that expected for emission from aligned grains. However, scattering and emission signals would have to cancel nearly perfectly in order to account entirely for the low observed polarization fraction. Nevertheless, there are promising candidates to describe how the suppression of polarized emission might have occurred. Cho & Lazarian (2007) assume 100% efficient alignment of grains with the magnetic field in regions of the disk where the alignment criterion is met, which is overly optimistic and now known to be unrealistic (see discussion in Section 4.2.2). In light of the recent work on the quantitative theory of grain alignment (Lazarian & Hoang 2007; Hoang & Lazarian 2008, 2009), the Cho & Lazarian (2007) result may be considered an upper limit to the theoretical expectation for the polarization properties of disks. A reduction to 10% efficiency, which is within the expectations based on recent developments in grain alignment theory, could alone explain the low polarization fraction observed. Another possibility is that the grains contributing most of the polarized emission in the model are well (or not so well) aligned, but rounder than the cross section ratio assumed in the initial model and therefore inefficient emitters of polarized radiation. This is also reasonable based on a rough estimate of the timescales and shapes expected for collisional growth of elongated ISM grains.

While each of these factors would have to be substantially different from what is expected in the initial model to alone account for the low polarization fraction, it is of course entirely possible that several effects are playing a combined role. For example, grains with a cross section ratio of 1.5 instead of 2.1 could combine with a 50% alignment efficiency to account entirely for the difference between observations and models. A small degree of field tangling (expected because of turbulence in the disk) could further reduce the expected polarization signature. While we cannot constrain precisely which factors are contributing in which proportions to the suppression of polarization in the disks observed with the SMA, we identify these three factors (grain elongation, alignment efficiency, and field tangling) as the most plausible sources of the suppression of polarized emission. They produce the greatest change in polarization properties within a reasonable range of parameter values, and there exists a theoretical justification for why they should exist, even if the magnitude of the effect is not well constrained.

Future observations with higher sensitivity may be able to disentangle these effects to some extent, particularly the degree of field tangling. It would also be useful to obtain high spatial resolution observations of the disks with tentative detections of a 2%–3% polarization fractions to confirm the strength and origin of the emission on small spatial scales, and to expand the sample size in order to determine whether the low polarization fraction constrained by the SMA is universal for disks around young stars.

We thank Alyssa Goodman for helpful conversations that improved the manuscript. Partial support for this work was provided by NASA Origins of Solar Systems Program Grant NAG5-11777. A.M.H. acknowledges support from a National Science Foundation Graduate Research Fellowship. Support for S.M.A. was provided by NASA through Hubble Fellowship grant no. HF-01203-A awarded by the Space Telescope Science Institute, which is operated by the Association of Universities

for Research in Astronomy, Inc., for NASA, under contract NAS 5-26555.

## REFERENCES

- Aannestad, P. A., & Purcell, E. M. 1973, *ARA&A*, **11**, 309
- Aitken, D. K., Efstathiou, A., McCall, A., & Hough, J. H. 2002, *MNRAS*, **329**, 647
- Alexander, R. D., & Armitage, P. J. 2007, *MNRAS*, **375**, 500
- Balbus, S. A., & Hawley, J. F. 1991, *ApJ*, **376**, 214
- Balbus, S. A., & Hawley, J. F. 1998, *Rev. Mod. Phys.*, **70**, 1
- Balbus, S. A., Hawley, J. F., & Stone, J. M. 1996, *ApJ*, **467**, 76
- Boss, A. P. 2004, *ApJ*, **616**, 1265
- Calvet, N., D'Alessio, P., Hartmann, L., Wilner, D., Walsh, A., & Sitko, M. 2002, *ApJ*, **568**, 1008
- Chambers, J. E. 2006, *ApJ*, **652**, L133
- Chandrasekhar, S. 1960, *Proc. Natl. Acad. Sci. USA*, **46**, 253
- Chiang, E. I., Jöng, M. K., Creech-Eakman, M. J., Qi, C., Kessler, J. E., Blake, G. A., & van Dishoeck, E. F. 2001, *ApJ*, **547**, 1077
- Cho, J., & Lazarian, A. 2005, *ApJ*, **631**, 361
- Cho, J., & Lazarian, A. 2007, *ApJ*, **669**, 1085
- Ciesla, F. J. 2007, *Science*, **318**, 613
- D'Alessio, P., Calvet, N., & Hartmann, L. 1997, *ApJ*, **474**, 397
- Dolginov, A. Z. 1972, *Ap&SS*, **18**, 337
- Dolginov, A. Z., & Mitrofanov, I. G. 1976, *Ap&SS*, **43**, 291
- Draine, B. T., & Weingartner, J. C. 1996, *ApJ*, **470**, 551
- Dullemond, C. P., & Dominik, C. 2005, *A&A*, **434**, 971
- Girart, J. M., Rao, R., & Marrone, D. P. 2006, *Science*, **313**, 812
- Grady, C. A., et al. 2000, *ApJ*, **544**, 895
- Greenberg, J. M. 1968, *Interstellar Grains*, ed. B. M. Middlehurst & L. H. Aller (Chicago, IL: Univ. of Chicago Press), 221
- Hartmann, L., Calvet, N., Gullbring, E., & D'Alessio, P. 1998, *ApJ*, **495**, 385
- Hildebrand, R. H., & Draganov, M. 1995, *ApJ*, **450**, 663
- Hildebrand, R. H., Davidson, J. A., Dotson, J. L., Dowell, C. D., Novak, G., & Vaillancourt, J. E. 2000, *PASP*, **112**, 1215
- Hoang, T., & Lazarian, A. 2008, *MNRAS*, **388**, 117
- Hoang, T., & Lazarian, A. 2009, *ApJ*, **697**, 1316
- Hoff, W., Henning, T., & Pfau, W. 1998, *A&A*, **336**, 242
- Hughes, A. M., Wilner, D. J., Calvet, N., D'Alessio, P., Claussen, M. J., & Hogerheijde, M. R. 2007, *ApJ*, **664**, 536
- Hughes, A. M., Wilner, D. J., Qi, C., & Hogerheijde, M. R. 2008, *ApJ*, **678**, 1119
- Isella, A., Testi, L., Natta, A., Neri, R., Wilner, D., & Qi, C. 2007, *A&A*, **469**, 213
- Kitamura, Y., Kawabe, R., & Saito, M. 1996, *ApJ*, **457**, 277
- Krejny, M., Matthews, T., Novak, G., Cho, J., Li, H., Shinnaga, H., & Vaillancourt, J. E. 2009, arXiv:0903.1255
- Lay, O. P., Carlstrom, J. E., & Hills, R. E. 1997, *ApJ*, **489**, 917
- Lazarian, A. 2007, *J. Quant. Spectrosc. Radiat. Transfer*, **106**, 225
- Lazarian, A., & Hoang, T. 2007, *ApJ*, **669**, L77
- Lazarian, A., & Hoang, T. 2008, *ApJ*, **676**, L25
- Lee, H. M., & Draine, B. T. 1985, *ApJ*, **290**, 211
- Lynden-Bell, D., & Pringle, J. E. 1974, *MNRAS*, **168**, 603
- Mamajek, E. E. 2005, *ApJ*, **634**, 1385
- Mannings, V. 1994, *MNRAS*, **271**, 587
- Mannings, V., & Sargent, A. I. 1997, *ApJ*, **490**, 792
- Marrone, D. P. 2006, PhD thesis, Harvard Univ.
- Marrone, D. P., & Rao, R. 2008, *Proc. SPIE*, **7020**, 702001
- Mathis, J. S., Rumpl, W., & Nordsieck, K. H. 1977, *ApJ*, **217**, 425
- Muzerolle, J., Briceño, C., Calvet, N., Hartmann, L., Hillenbrand, L., & Gullbring, E. 2000, *ApJ*, **545**, L141
- Natta, A., Testi, L., Neri, R., Shepherd, D. S., & Wilner, D. J. 2004, *A&A*, **416**, 179
- Padoan, P., Goodman, A., Draine, B. T., Juvela, M., Nordlund, Å., & Rögnvaldsson, Ö. E. 2001, *ApJ*, **559**, 1005
- Qi, C., et al. 2004, *ApJ*, **616**, L11
- Roberge, A., Weinberger, A. J., & Malumuth, E. M. 2005, *ApJ*, **622**, 1171
- Sano, T., Miyama, S. M., Umebayashi, T., & Nakano, T. 2000, *ApJ*, **543**, 486
- Schneider, G., Wood, K., Silverstone, M. D., Hines, D. C., Koerner, D. W., Whitney, B. A., Bjorkman, J. E., & Lowrance, P. J. 2003, *AJ*, **125**, 1467
- Semenov, D., Wiebe, D., & Henning, T. 2006, *ApJ*, **647**, L57
- Shakura, N. I., & Sunyaev, R. A. 1973, *A&A*, **24**, 337
- Shu, F. H., Galli, D., Lizano, S., Glassgold, A. E., & Diamond, P. H. 2007, *ApJ*, **665**, 535

- Tamura, M., Hough, J. H., Greaves, J. S., Morino, J.-I., Chrysostomou, A., Holland, W. S., & Momose, M. 1999, [ApJ](#), **525**, 832
- Tamura, M., Hough, J. H., & Hayashi, S. S. 1995, [ApJ](#), **448**, 346
- Turner, N. J., Sano, T., & Dziourkevitch, N. 2007, [ApJ](#), **659**, 729
- van den Ancker, M. E., de Winter, D., & Tjin A Djie, H. R. E. 1998, [A&A](#), **330**, 145
- Velikhov, E. P. 1959, *Sov. Phys.—JETP*, **36**, 1398
- Vrba, F. J., Coyne, G. V., & Tapia, S. 1993, [AJ](#), **105**, 1010
- Wardle, M. 2007, [Ap&SS](#), **311**, 35
- Webb, R. A., Zuckerman, B., Platais, I., Patience, J., White, R. J., Schwartz, M. J., & McCarthy, C. 1999, [ApJ](#), **512**, L63
- Weidenschilling, S. J. 1988, in *Formation Processes and Time Scales for Meteorite Parent Bodies*, ed. J. F. Kerridge & M. S. Matthews (Tucson, AZ: Univ. of Arizona Press), 348
- Weintraub, D. A., Sandell, G., & Duncan, W. D. 1989, [ApJ](#), **340**, L69
- Wilner, D. J., D'Alessio, P., Calvet, N., Claussen, M. J., & Hartmann, L. 2005, [ApJ](#), **626**, L109
- Wright, C. M. 2007, [Ap&SS](#), **311**, 47